On the Importance of Including Cohesive Zone Models in modelling mixed-mode Aneurysm Rupture

Concannon J[1], Ó Máirtín É[1], FitzGibbon B[1], Hynes N[2], Sultan S[2], McGarry JP[1]

[1] Biomedical Engineering, College of Engineering and Informatics, National University of Ireland Galway

[2] Department of Vascular and Endovascular Surgery, Galway University Hospitals

Corresponding author: jamie.concannon@nuigalway.ie

Abstract

The precise mechanism of rupture in AAAs has not yet been uncovered. The phenomenological failure criterion of the coefficient of proportionality between von Mises stress and tissue strength does not account for any mechanistic foundation of tissue fracture. Experimental studies have shown that arterial failure is a stepwise process of fibrous delamination (mode II) and kinking (mode I) between layers. Such a mechanism has not previously been considered for AAA rupture. In the current study we consider both von Mises stress in the wall, in addition to interlayer tractions and delamination using cohesive zone models. Firstly, we present a parametric investigation of the influence of a range of AAA anatomical features on the likelihood of elevated interlayer traction and delamination. We observe in several cases that the location of peak von Mises stress and tangential traction coincide. Our simulations also reveal however, that peak von Mises and intramural tractions are not coincident for aneurysms with Length/Radius less than 2 (short high-curvature aneurysms) and for aneurysms with symmetric ILT. Additionally, we present three patient-specific AAA models derived directly from CT scans, which also illustrate that the location of von Mises stress does not correlate with the point of interlayer delamination, suggesting that incorporating cohesive zone models into clinical based FE analyses may capture a greater proportion of ruptures *in-silico*.

Introduction

The reliable evaluation of the rupture risk of a specific abdominal aortic aneurysm (AAA) does not currently exist. Nearly all of the criteria which are used by clinicians to indicate the need for surgical intervention are based on empirical data (Vorp, 2007). A number of finite element frameworks have been proposed in an attempt to improve AAA rupture risk estimates based on stress computations, however their ability to accurately predict rupture locations is just over 50% (Erhart et al., 2016). AAAs are deemed common in the general population with a global prevalence of 4.8%, and an 80% mortality rate in the event of rupture (Li et al., 2013). With the affected cohort generally presenting with several comorbidities that often render surgical treatment also life threatening, this presents a significant challenge to surgeons who search for reliable measures to weigh the risk of rupture versus risk of perioperative death to patients.

The maximum AAA diameter has widely been used to justify the need for surgical intervention, with AAAs greater than 5.5 cm in diameter deemed to require elective surgery (Kontopodis et al., 2016). However, clinical studies conducted by Darling et al., and Hall et al., determined that rupture rates of between 12% and 23% have been reported for AAAs less than 5 cm in diameter and rupture rates of 40% have been reported for AAAs greater than 5 cm (Darling, 1977, Hall, 2000). Such a method is clearly lacking in mechanistic foundation, as evident in the more recent drive towards computational based methods of rupture risk (Fillinger et al., 2003; Polzer and Gasser, 2015; Venkatasubramaniam et al., 2004; Xenos et al., 2014). Most of these models have involved predicting the magnitude and location of peak von Mises stress (σ_{vm}) in the AAA wall and using this as a predictor for rupture. A rupture potential index (RPI) has also been proposed based on the ratio of computed wall stress to an estimate of wall strength (based on factors such as family history, gender, AAA diameter and intraluminal thrombus (ILT) thickness) (Vande Geest et al., 2006). It was reported by the same authors that ILT is present in approximately 75% of AAAs (Vande Geest, 2006) and models incorporating ILT result in significant changes in both the magnitude and location of σ_{vm} in the AAA wall compared to simpler models where the ILT is omitted (Doyle et al., 2007). Although these phenomenological models have provided advance in terms of clinical integration of computational methods, they can only predict an accurate rupture location in 53.8% of cases (Erhart et al., 2016), and provide little in terms of insight into the mechanics of rupture/delamination of the arterial tissue.

Accurate *in-silico* predictions of rupture potential indices rely on an in depth understanding of the process involved. Haslach et al., reported a stepped rupture surface following pressure inflation of rings of arterial tissue (Figure 1(b)), and subsequently state that tension experiments do not provide an accurate characterization of aortic rupture nor a valid useful measure of the *in-vivo* aortic rupture stress. The same experiment was carried out on a healthy un-notched ring sample, indicating that the tissue need not be 'diseased' for rupture to occur via intramural delamination (Haslach et al., 2018). It is generally accepted that medial degeneration is an essential prerequisite for interface delamination (Hirst et al., 1958), which indeed may reduce the pressures required to induce a mixed mode-type failure. Rabin and Haslach, (2018) found that the propagation length was longer in aneurysmal versus healthy aortic tissues (6.60 ± 4.19 mm vs 2.27 ± 1.20 mm) a result which is in agreement with the significantly lower resistance to delamination found in aneurysmal human ascending thoracic aortas compared with healthy tissues by Pasta et al., (2012). Additionally, no intimal tear is found in up to 12% of aortic dissections indicating the possibility of rupture due to an initial intramural failure (Brunet et al., 2020).

Others have also reported a jagged or kinked appearance of the rupture surface. The existence of delamination planes at the rupture zone following tension-inflation inside an X-ray microtomography setup were reported by Brunet et al., (2020) (Figure 1(c)). FitzGibbon and McGarry (2020) also report a step-wise interface delamination of aortic tissue when subject to a ring pull test (Figure 1(a)). Dissection-like rupture was found in most burst-inflation samples by Romo et al., (2014) who also report that rupture often initiated at a different location to the peak stress, while similar experiments by Kim et al., (2012) revealed in certain cases that delamination occurred before AAA rupture. Bellini et al., (2017) showed in mice with impaired collagen fibrillogenesis (TSP2-null), that although biaxial mechanical tests were not different compared to controls, failure tests confirmed that the pressure at which the aorta ruptures is significantly lower in TSP2-null mice compared to age-matched controls (640±37 vs. 1120±45 mmHg). Moreover, all 40-week-old mutant aortae failed by delamination, not rupture. The jagged plateau region of load-extension plots performed by Pasta et al., (2012) & Purslow, (1983) suggests that rupture does not propagate at a steady rate but arrests and reinitiates at somewhat regular intervals reflecting the fibrous nature of the wall. Helfenstein-Didier et al., (2018) describes a similar pattern of rupture in porcine aortic samples of; mode I failure of musculo-elastic units followed by mode II separation of the same layer from the wall. Furthermore as reported by (Haslach et al., 2015), if tissue failure were solely due to tension-driven mode I crack opening, radial crack propagation from the tip of the cut notch would be

expected, as opposed to the circumferential/longitudinal propagations observed throughout the literature (Brunet et al., 2020; Haslach et al., 2011; Hirst et al., 1958; Rabin and Haslach, 2018; Sugita and Matsumoto, 2018). Substantiating this point is the fact that a significant volume of literature report on '*dissecting aneurysms*', a distinct pathological condition from traditional aneurysms and dissections (Bersi et al., 2020; Cho et al., 2019; Hakimi and Sivakumar, 2019; Maus et al., 2018; Phillips et al., 2017; Schriefl et al., 2012; Trachet et al., 2017; Xanthoulea et al., 2009). Altogether, these studies suggest that intramural delamination should be investigated as a potentially important factor in the process of AAA rupture.

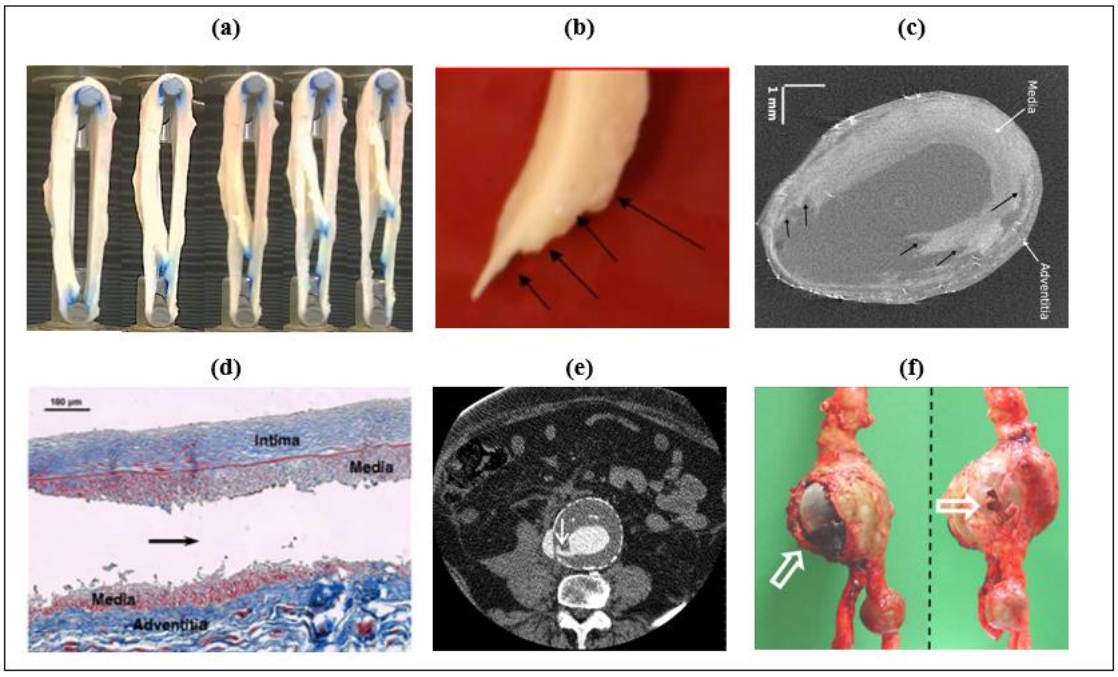

Figure 1: (a) Kinking intramural fracture of aortic tissue during ring pull test (FitzGibbon and McGarry 2020). (b) Step rupture surface in a ring sample shows sequential separation between adjacent radial and then circumferential fascicles (Halsach et al., 2011). (c) Delamination planes at the rupture zone following tension-inflation inside an X-ray microtomography setup (Brunet et al., 2020). (d) Histological evidence of jagged arterial delamination within the medial layer (Wang et al., 2014). (e) Contrast Enhanced CT image of impending AAA rupture with stepped rupture surface (Schartz et al., 2007). (f) Complex failure of patient-specific AAA wall (Raghavan et al., 2011).

In this study, interface delamination between the individual wall layers of the AAA is investigated using Cohesive Zone Models (CZMs). Cohesive zone formulations have previously been implemented to model the propagation of arterial dissection and plaque rupture during balloon angioplasty intervention (Ferrara and Pandolfi, 2008; Gasser and Holzapfel, 2007). However, cohesive zone modelling has not previously been used to predict interlayer delamination in AAAs. Firstly, we present a parametric investigation of the influence of a range of AAA anatomical features on the likelihood of elevated interlayer traction and delamination.

We observe in several cases that the location of peak σ_{vm} and tangential traction (T_t) coincide. Our simulations also reveal however, that peak σ_{vm} and intramural tractions are not coincident for aneurysms with Length/Radius less than 2 (short high-curvature aneurysms) and for aneurysms with symmetric ILT. Additionally, we present three patient-specific AAA models derived directly from CT scans, which also illustrate that the location of σ_{vm} does not correlate with the point of interlayer delamination. Against the backdrop of current AAA rupture risk frameworks only achieving accurate predictions for rupture in 53.8% of cases, it appears that there may be use for incorporating cohesive zone models into clinical based FE analyses to capture a greater proportion of ruptures/dissections *in-silico*.

Methodology

In order to investigate the relationship between interface traction and σ_{vm}, a series of parametric investigations on the influence of a range of AAA anatomical features on the likelihood of elevated interlayer traction and delamination were performed, each of which were subject to the same internal pressure and boundary conditions. We then present three patient-specific aneurysm simulations derived directly from CT scans. The following subsections describe the idealised and patient-specific methodologies.

2.1 Idealised Cases

A series of finite element models were created using MATLAB (R2017b, MathWorks Inc., Natick, MA, USA) based on a sigmoid function where the radius of the vessel is a function of the axial position along the aneurysm length (**Figure 2**). By altering the parameters of the sigmoid function we investigate the effect of the following conditions on the interface traction/$\boldsymbol{\sigma_{vm}}$ relationship; (i) aneurysm curvature, (ii) aneurysm width, (iii) aneurysm skewness, (iv) aneurysm ellipticity, (v) symmetric and asymmetric ILT, and (vi) vessel anisotropy (**Figure 3**).

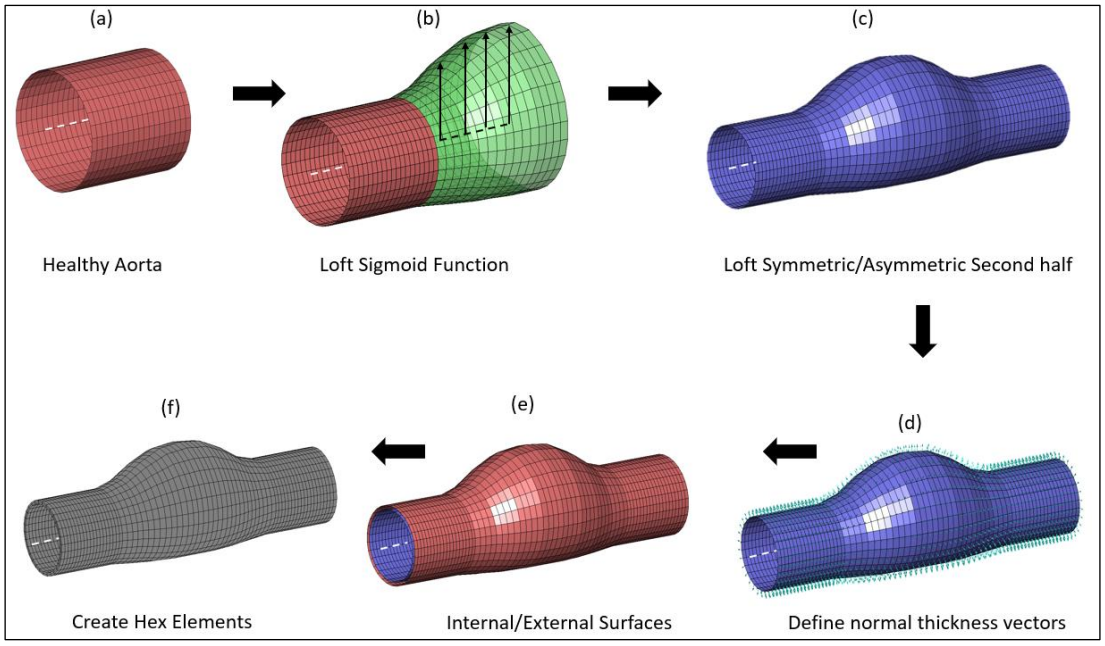

Figure 2: Flowchart describing idealised parametric study mesh creation. (a) An initial loft is performed along the healthy proximal aortic segment to the point of the aneurysm neck. (b) A sigmoid function describes the aneurysm width as a function of the axial location in space. This is lofted onto the previously generated healthy aortic segment from (a). (c) The second half of the aneurysm mesh is created in a similar manner with allowable symmetric/asymmetric constraints. (d) The element normal thickness vectors are defined which allows creation of the external surface elements (e), and finally hexahedral elements are created between the two surfaces to define the final aneurysm mesh (f).

The following cases were investigated; (a) Curvature (L/R) – where R (radius) is fixed at 20mm and L (length)= [50mm, 40mm, and 30mm] defined by the c_2 parameter in the sigmoid function, (b) Width (W_1) where W_1=R*S, (R=20mm, S=[1.00, 0.66, 0.33]) and is implemented through a radial shrinkage of the lumen coordinates by the factor S prior to pressure inflation. (c) Skewness ($C_{2,1}/C_{2,2}$), where C_{21} =7 and C_{22}=[7, 11, 15] which defines the degree of axial asymmetry along the aneurysm length. (d) Ellipticity (W_1/W_2), where W_1 is as previously defined above and W_2 =[1.00, 0.90, 0.80], which is implemented through a circumferentially descending multiplicator that is applied to the lumen coordinates to achieve varying degrees of aneurysm ellipticity. (e) ILT (symmetric/asymmetric), symmetric ILT is simply achieved by offsetting the internal lumen coordinates inwards by the symmetric ILT thickness t_1. Asymmetric ILT is achieved by defining the internal lumen and filling the void between the lumen surface and the internal wall surface with tetrahedral elements using GIBBON (Moerman, 2018).

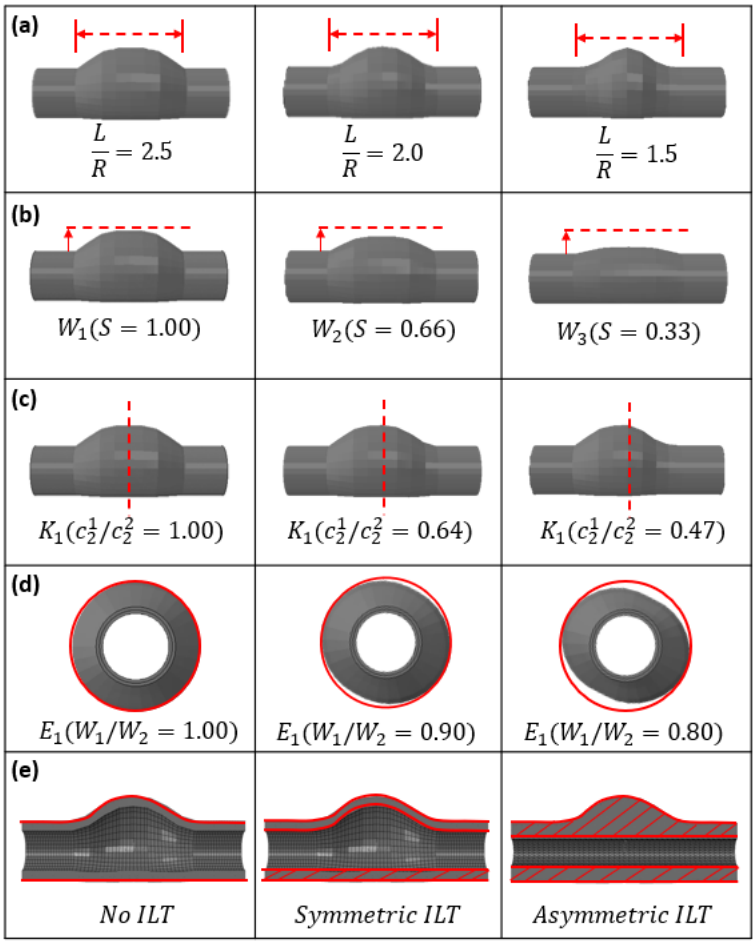

Figure 3: Idealised parametric study geometries created using Matlab. (a) Curvature (L/R) – where R is fixed at 20mm and L= [50mm, 40mm, and 30mm], (b) Width (W_1) where W_1=R*S, (R=20mm, S=[1.00, 0.66, 0.33]). (c) Skewness ($C_{2,1}/C_{2,2}$), where C_{21} =7 and C_{22}=[7, 11, 15]. (d) Ellipticity (W_1/W_2), where W_1 is as previously defined above and W_2 =[1.00, 0.90, 0.80]. (e) ILT (symmetric/asymmetric).

Vessel Anisotropy:

Material anisotropy is considered using a bilinear type formulation (Fereidoonnezhad et al., 2020) where the strain energy function is given as

$$\Psi_{\text{tot}} = \Psi_{\text{iso}} + \Psi_{aniso}$$

$$\Psi_{aniso} = \sum_{i=1,2} \begin{cases} E_{1f}\left(\frac{2}{3}\lambda_{fi}^3 - \lambda_{fi}^2 + \frac{1}{3}\right) & \lambda_{fi} - 1 \le D_{1f} \\ \frac{2}{3}\lambda_{fi}^3\left(q_f - 2p_f\right) + \frac{p_f}{2}\lambda_{fi}^4 + \lambda_{fi}^2\left(p_f - q_f + r_f\right) + \psi_{01} & D_{1f} < \lambda_{fi} - 1 < D_{2f} \\ \frac{2E_{2f}}{3}\lambda_{fi}^3 + \lambda_{fi}^2\left(p_f D_{2f}^2 + q_f D_{2f} + r_f - E_{2f} - E_{2f}D_{2f}\right) + \psi_{02} & \lambda_{fi} - 1 \ge D_{2f} \end{cases}$$

where

$$p_f = (E_{1f} - E_{2f})/2(D_{1f} - D_{2f})$$

$$q_f = E_{1f} - 2D_{1f}p_f$$

$$r_f = (E_{1f} - q_f)D_{1f} - p_f D_{1f}^2$$

and ψ_{01} and ψ_{01} are two constants which ensure the continuity of strain energy. E_{1f} and E_{2f} are slopes of the linear regimes, D_{1f} and D_{2f} are the values of the nominal fibre strain at the end of the first linear regime and at the beginning of the second linear regime. The bilinear strain-stiffening fibre model is placed in parallel with a linear neo-Hookean matrix

$$\Psi_{iso}(\mathbf{C}) = \frac{K}{2}(J-1)^2 + \frac{\mu}{2}(\bar{I}_1 - 3)$$

where K is the effective bulk modulus, μ is the effective shear modulus, and $\bar{I}_1$ is the first invariant of the isochoric right Cauchy-Green Tensor ($\bar{\mathbf{C}} = J^{-\frac{2}{3}}\mathbf{C}$).

A Levenberg-Marquardt based optimization algorithm is used to determine the parameters that fit the experimental data. **Figure 4** below shows the simulated stress-strain response (SIM) with the experimental data of Vande Geest et al., (2006) overlaid.

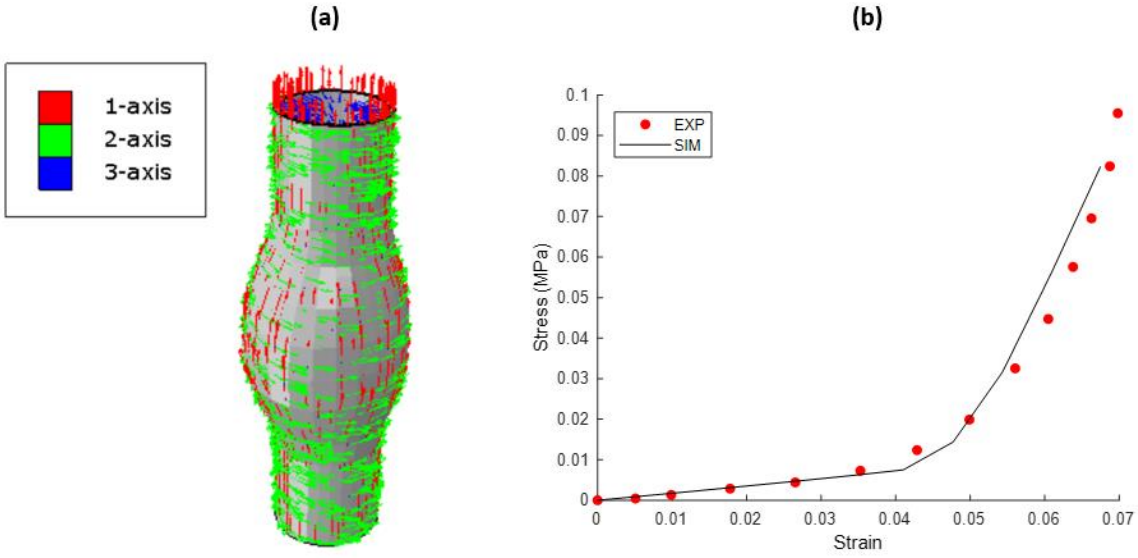

Figure 4: (a) Example of discrete fiber orientation applied to aneurysm model based on internal lumen surface and primary axis method. Collagen fibers are defined with respect to each individual element orientation and prescribed via the anisotropic material formulation such that the material captures the stress-strain response to AAA uniaxial tension experiments. (b) Experimental tension experiments of Vande Geest et al., (2006) (EXP) with finite element model result overlaid (SIM).

The interface between each artery wall layer is modelled using the non-potential-based SMC and NP2 CZMs presented in (Máirtín et al., 2014; McGarry et al., 2014) (SMC model is used in separation and NP2 model is used in compression/over-closure);

$$T_n(\Delta_n, \Delta_t) = \sigma_{max} exp(1) \left(\frac{\Delta_n}{\delta_n}\right) exp\left(-\sqrt{\frac{\Delta_n^2}{\delta_n^2} + \frac{\Delta_t^2}{\delta_t^2}}\right) \quad (1)$$

$$T_t(\Delta_n, \Delta_t) = \tau_{max} exp(1) \left(\frac{\Delta_t}{\delta_t}\right) exp\left(-\sqrt{\frac{\Delta_n^2}{\delta_n^2} + \frac{\Delta_t^2}{\delta_t^2}}\right) \quad (2)$$

where T_n is the traction in the normal direction; T_t is the traction in the tangential direction; Δ_n is the normal component of the interface separation vector; Δ_t is the tangential component of the interface separation vector; σ_{max} is the normal interface strength; τ_{max} is the tangential interface strength; δ_t is the tangential interface characteristic length; and δ_n is the normal interface characteristic length. Values of maximum interface strengths in the normal (σ_{max}) and tangential (τ_{max}) directions are based on dissection experiments of human aortic tissue following autopsy (Sommer, 2008). Specifically, an interaction strength of $\sigma_{max} = \tau_{max} = 16kPa$ and a critical cohesive interface length of $\delta_c = 10\mu m$ is chosen.

2.2 Patient-Specific Cases

Patient-specific CT scans (1.25 mm slice thickness) were obtained with permission from the Western Vascular Institute, University College Hospital, Galway. DICOM (Digital Imaging and Communication in Medicine) files containing the CT data were imported into Mimics© (v14.11, Materialise, Belgium), a specialised image processing software, for segmentation and reconstruction. An illustration summarising the reconstruction process, from CT scans to final geometry, is shown in **Figure 5**. A thresholding range was first chosen to ensure the incorporation of the entire ILT (a CT slice of the original geometry is shown in **Figure 5(c)**). After the creation of the initial geometry, each CT slice was carefully examined and edited to establish a more accurate model of the ILT geometry (**Figure 5(d)**). Additionally, a number of smoothing iterations were performed to remove sharp edges and other surface artefacts. The integrity of the final AAA geometry was ensured by creating a polyline representation of the AAA geometry. Any discontinuity in a polyline indicated that additional reconstruction iterations were required (**Figure 5(e)**). The polyline growing tool was utilised to ensure that there were no holes present in the geometry. Fifteen control points (a measure of the number of smoothing iterations performed) per slice, were chosen based on previous work which established the optimum number of control points required without losing geometry accuracy

(Doyle et al., 2007). The final reconstructed 3D geometry of the ILT (for Patient A), including the vertebral column, is shown in **Figure 5(f)**. In total, three AAA geometries, shown in **Figure 5(g,h,i)**, were analysed. For the remainder of this study these AAA geometries will be referred to as Patient A, Patient B and Patient C.

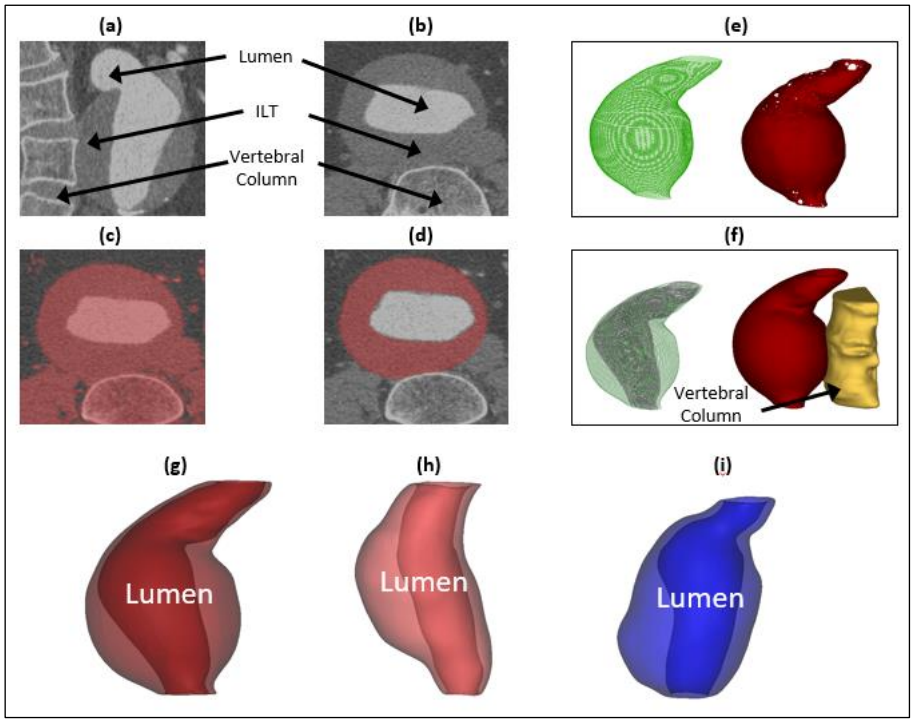

Figure 5: Outline of the reconstruction steps taken to create final AAA geometry. CT scans of the aneurysm (Patient A) in the sagittal and transverse planes are shown in (a) and (b) respectively. The initial and final aneurysm 'mask' in the transverse plane is shown in (c) and (d) respectively. The initial and final 3D AAA geometry together with surface polylines is shown in (e) in (f) respectively with the position of the vertebral column also indicated. (g,h,i) indicate final AAA geometries (1,2,3) for three clinical cases.

After importing the ILT geometry into Abaqus, intima, media and adventitia layers were generated by offsetting the geometry from the abluminal surface of the ILT. In each of the idealised and patient-specific cases the individual layer thicknesses are based on those reported in Concannon et al., (2019). A slightly-compressible Neo-Hookean hyperelastic constitutive formulation is utilised to describe the AAA wall layers and intraluminal thrombus. The properties for each wall layer are estimated from published properties of arteries (Gao et al., 2006; Kohn et al., 2015; Teng et al., 2015). Unless otherwise stated, the effective stiffness of the intima, media and adventitia layers are 2.9MPa, 1.8MPa and 10.8MPa respectively. The properties of the intraluminal thrombus (ILT) are based on the study of (Wang, 2001) with a stiffness of 0.428MPa assigned to the ILT in this study. An internal pressure of 200mmHg is applied to simulate blood pressure acting on the AAA wall. The AAA geometry is partially constrained in the proximal and distal regions, representing the crux of the diaphragm and the

common iliac bifurcation *in-vivo*. A tie constraint is applied between the aneurysm and the vertebral column surfaces. An increase in finite element mesh density from 5000 to 50000 elements results in only a ~1% increase in the computed wall stress. Therefore, a mesh density of 5000 elements is used for all analyses presented in this study. Hexahedral elements were used to ensure high accuracy at the interface.

Results

We first investigate a suite of parameterised geometries that capture the typical spectrum of AAAs which present clinically and observe in most cases that the location of peak σ_{vm} and T_t coincide. There are, however, certain cases where the locations do not coincide, which suggests that a cohesive zone model should be used in addition to σ_{vm} in finite element-based rupture risk models. Additionally, we present three patient-specific AAA models derived directly from CT scans, which also illustrate that the location of peak σ_{vm} does not correlate with the point of interlayer delamination.

3.1 Idealised Cases

Aneurysm Curvature (L/R):

The baseline geometry in each case is presented in the first row of **Figures 6-11**, and consists of an anteriorly distending AAA, with a width (R) (in-plane distance from central axis to anterior bulge) of 20mm, axial length (L) of 50mm, wall thickness of 1mm, and healthy proximal and distal segments of 10mm radius and 20mm length. **Figure 6** illustrates the effects of altering the curvature (L/R) of the aneurysm on the σ_{vm}/T_t relationship. In the baseline geometry (L/R=2.5), the peak σ_{vm}/T_t locations are coincident, at the aneurysm neck. For an aneurysm with (L/R=2.0), the peak σ_{vm} moves slightly towards the origin while the peak T_t is near the peak bulge with a separation distance of ~17mm. Similarly, for an aneurysm with (L/R=1.5), the peak σ_{vm} moves slightly closer again to the origin, while the peak T_t is near the peak bulge with a separation distance of ~22mm.

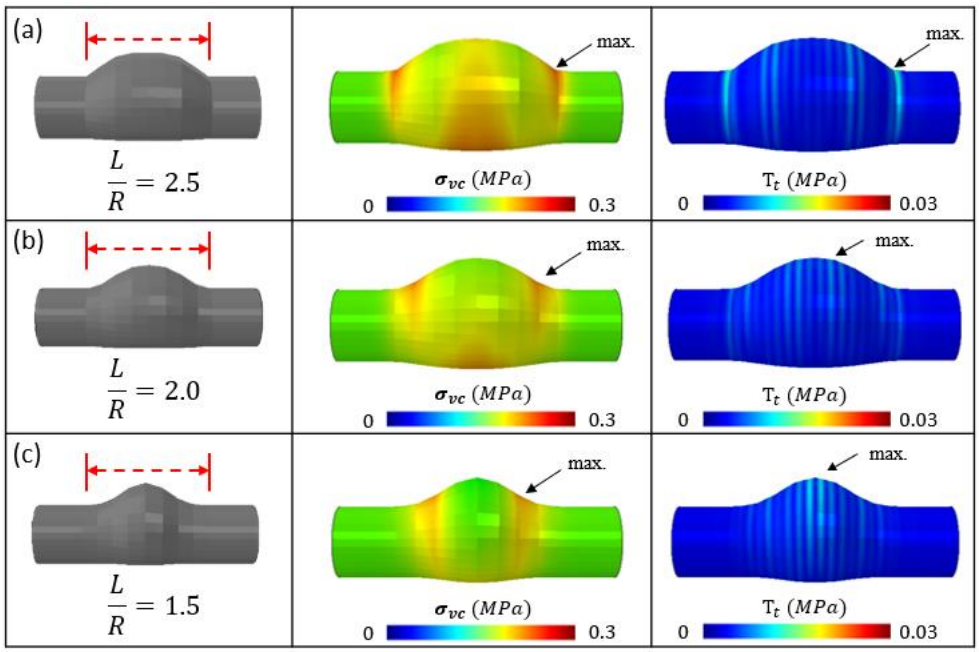

Figure 6: Effect of Curvature (L/R) on the peak σ_{vm}/T_t relationship. (a) Baseline geometry (L/R=2.5): peak σ_{vm} and T_t are coincident at the aneurysm neck. (b) L/R=2.0: peak σ_{vm} and T_t are not-coincident, and (c) L/R=1.5: peak σ_{vm} and T_t are not-coincident.

Aneurysm Width (W_1):

Next, we investigated the effect of varying the aneurysm width on the peak σ_{vm}/T_t relationship. In each case ($W_1 = 1.00, 0.66, 0.33$), although the peak σ_{vm} and T_t values reduce with decreasing aneurysm width, they remain coincident at the aneurysm neck (**Figure 7**).

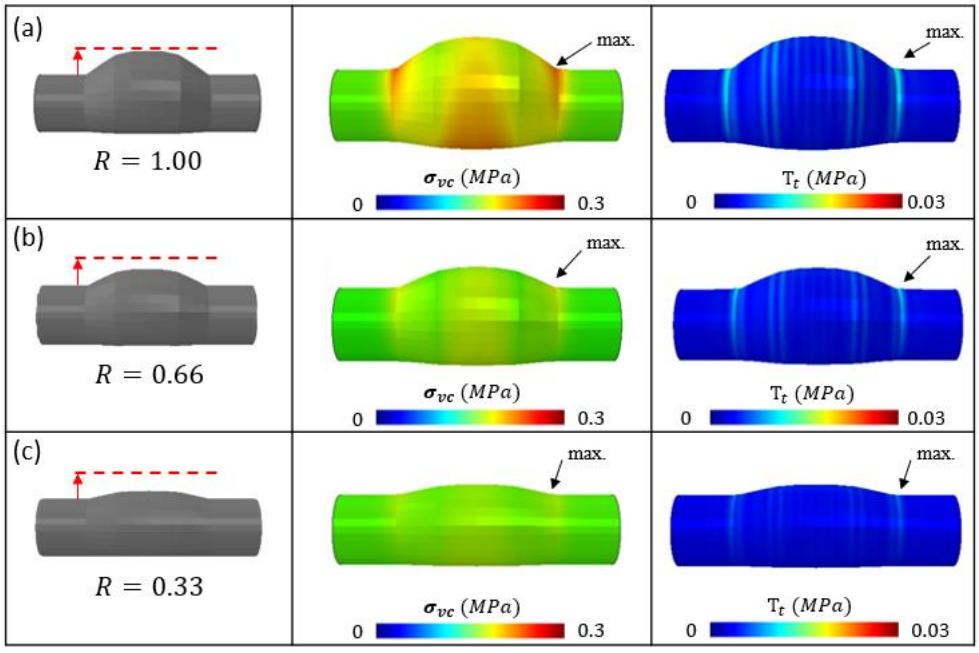

Figure 7: Effect of Width (W_1) on the peak σ_{vm}/T_trelationship. (a) Baseline geometry ($W_1 = 1.00$), (b) $W_1 = 0.66$, and (c) $W_1 = 0.33$. In each case the peak σ_{vm} and T_t are coincident at the aneurysm neck, and L=50mm.

Aneurysm Skewness ($C_{2,1}/C_{2,2}$):

By altering the ratio of the $C_{2,1}$ to $C_{2,2}$ parameters in the sigmoid function, the skewness of the aneurysm can be altered. In each case ($C_{2,1}/C_{2,2} = 1.00, 0.64, 0.47$) the peak σ_{vm} and T_t are coincident however their location follows the tighter radius of curvature at the aneurysm neck (**Figure 8**).

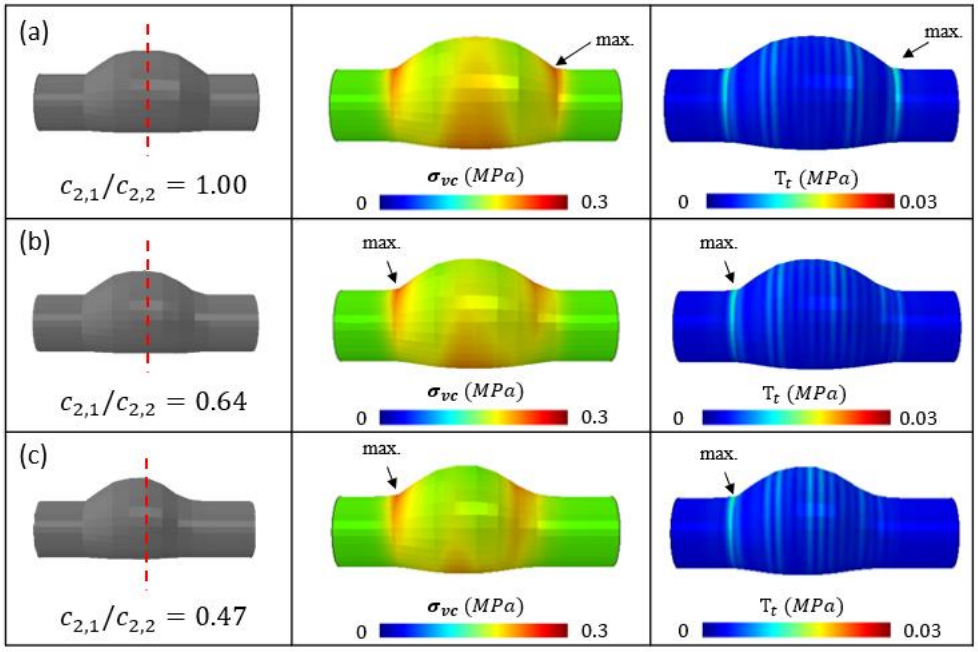

Figure 8: Effect of Skewness ($C_{2,1}/C_{2,2}$) on the peak σ_{vm}/T_t relationship. (a) Baseline geometry ($C_{2,1}/C_{2,2} = 1.00$), (b) $C_{2,1}/C_{2,2} = 0.64$, and (c) $C_{2,1}/C_{2,2} = 0.47$. In each case the peak σ_{vm} and T_t are coincident, however their location follows the tighter radius of curvature at the aneurysm neck, and $C_{2,1}$=7.

Aneurysm Ellipticity (W_1/W_2):

Next, we investigate aneurysm ellipticity and observe that σ_{vm} and T_t always coincide. In our baseline axisymmetric simulation (W_1/W_2=1.00) σ_{vm} and T_t are coincident and identical circumferentially at the aneurysm neck, as ellipticity increases (W_1/W_2=[0.90, 0.80]), both σ_{vm} and T_t decrease to a minimum at the minor axis width (**Figure 9**).

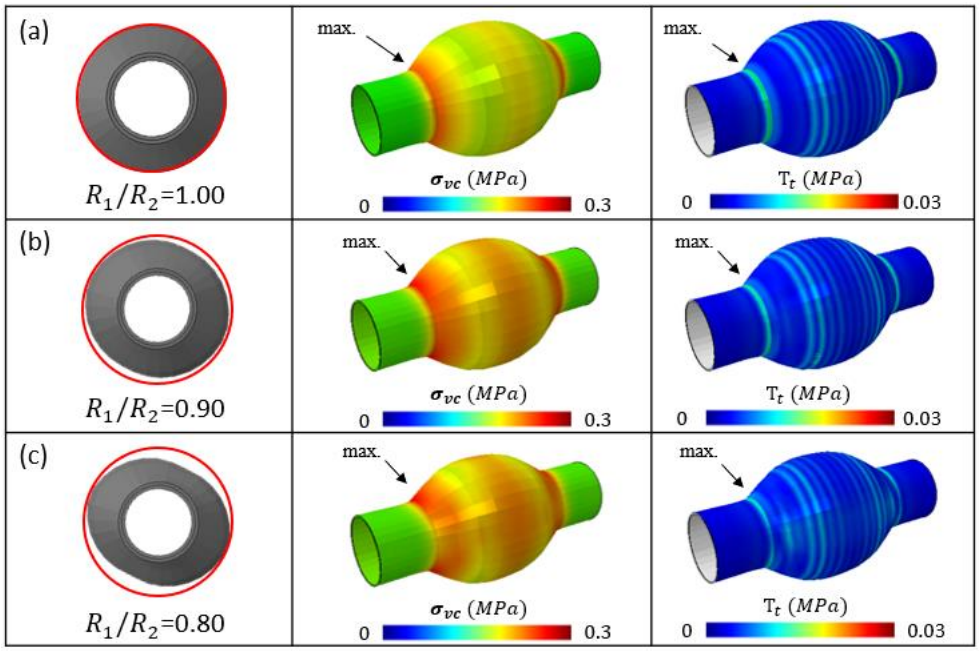

Figure 9: Effect of ellipticity (W_1/W_2) on the peak σ_{vm}/T_t relationship. (a) Baseline geometry ($W_1/W_2 = 1.00$), (b) $W_1/W_2 = 0.90$, and (c) $W_1/W_2 = 0.80$. In each case the peak σ_{vm} and T_t are coincident, however both decrease to a minimum at the minor axis width, and L/R=2.5.

Intraluminal Thrombus (ILT):

The presence of intraluminal thrombus has been reported previously as having a positive (Leung et al., 2006; Vorp and Vande Geest, 2005) and negative (Kazi et al., 2003; Speelman et al., 2010) effect on aneurysm rupture risk. Here we include both symmetric and asymmetric ILT in our parametric study. In the symmetric ILT case, the peak σ_{vm} and T_t do not coincide, with the σ_{vm} maximum at the aneurysm belly (point of maximum radius) while the T_t resides at the aneurysm neck (point at which healthy aorta and aneurysm meet). In the asymmetric ILT case, the peak σ_{vm} and T_t do coincide at the aneurysm neck. In each case here, L/R=2.5, and $C_{2,1}/C_{2,2}$=1.00 (**Figure 10**).

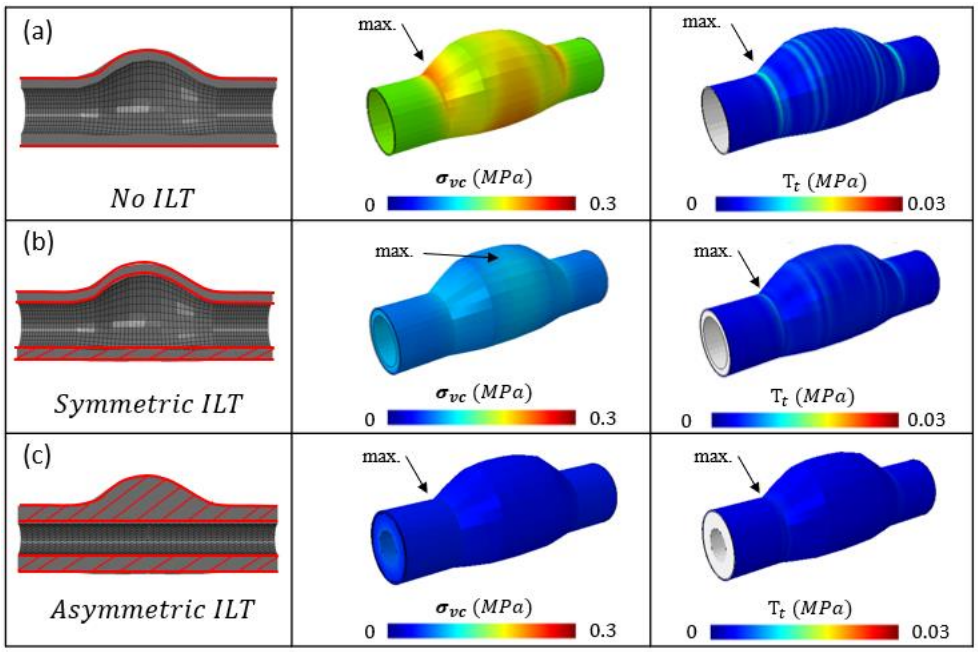

Figure 10: Effect of ILT on the peak σ_{vm}/T_t relationship. (a) Baseline geometry (No ILT), (b) Symmetric ILT, and (c) Asymmetric ILT. In the case of symmetric ILT, the peak σ_{vm} and T_t do not coincide, however in the case of asymmetric ILT they do at the aneurysm neck.

Finally, we investigate the effect of material anisotropy on the peak σ_{vm}/T_t relationship. By employing a bilinear type constitutive model that captures the strain-stiffening of collagen fibers we can capture the stress-strain behaviour of AAA tissue (Vande Geest et al., 2006). Applying these fitted parameters to the pressure inflation of the baseline AAA geometry, we observe that the peak σ_{vm} resides at the aneurysm belly in the anisotropic model whereas in the isotropic model it resides at the aneurysm neck. In both the isotropic and anisotropic case however the peak σ_{vm} and T_t are coincident (**Figure 11**).

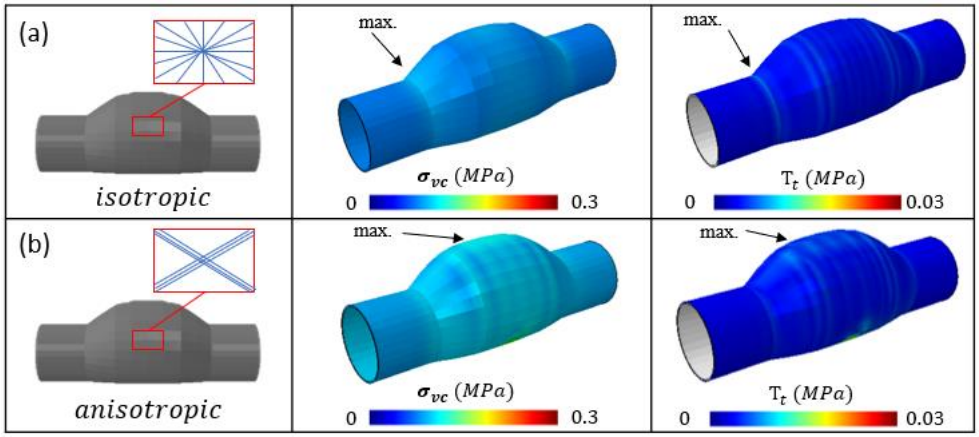

Figure 11: Effect of material anisotropy on the peak σ_{vm}/T_t relationship. (a) Baseline geometry (isotropic), (b) Baseline geometry (anisotropic). In the case of isotropic model, the peak σ_{vm} and T_t coincide at the aneurysm neck, however in the anisotropic model they coincide at the aneurysm belly.

3.2 Patient-specific Cases

Patient A:

The computed σ_{vm}/P distribution for Patient A, where individual AAA wall layer properties are assigned and an ILT is included, is shown in **Figure 12** in order to compare locations of σ_{vm}/P concentrations in the AAA wall with computed interface delamination locations. In **Figure 12** contour plots of the σ_{vm}/P distribution in the adventitia (**Figure 12**(**a**)) and media layer (**Figure 12**(**b**)) are presented, with a selection of nodes in the computed interface delamination patches highlighted for comparison of location (black circles). It is evident that the predicted location of interface delamination at the adventitial-medial (A-M) interface does not coincide directly with the location of maximum σ_{vm} in the adventitia layer (**Figure 12**(**a**)). Furthermore, predicted interface delamination at the intimal-medial (I-M) interface (**Figure 12**(**b**)) do not coincide with the peak σ_{vm} location in the media layer. In particular, the computed delamination location in the anterior region (circled) at the I-M interface coincides with a region in which the computed magnitude of σ_{vm} in the media layer is relatively low. It is important to note that initiation of delamination does not appreciably alter the distribution of σ_{vm}/P throughout the AAA wall. In contrast, when the ILT is neglected (**Figure 12**(**c**)), predicted interface delamination locations at the adventitia-media interface roughly coincide with the peak σ_{vm}/P region in the adventitia layer. This can be attributed to the fact that omission of the ILT leads to significant bending of the AAA geometry above the aneurysm neck, thereby inducing both high interlayer shear tractions and high σ_{vm}/P in this location.

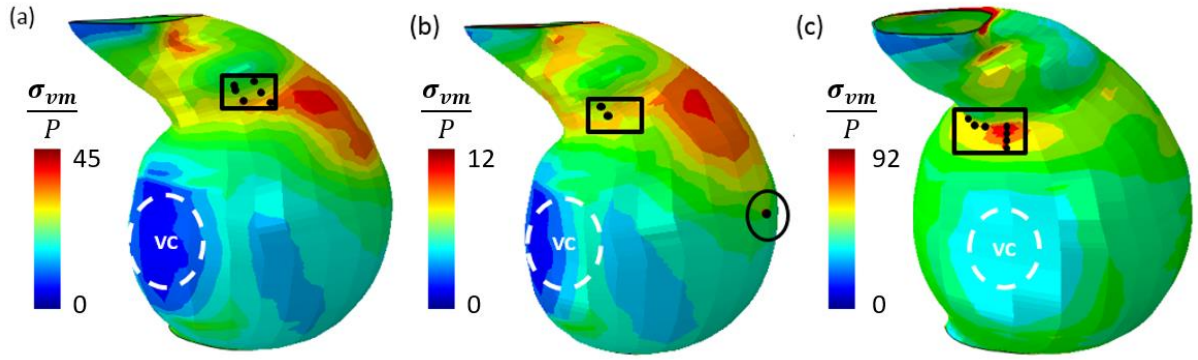

Figure 12: Distribution of computed von Mises stress over pressure in (a) the adventitia layer and (b) the media layer at an applied lumen pressure (P) of 150mmHg for Patient A. Computed regions of interface delamination do not coincide with areas of peak von Mises stress. (c) indicates the distribution of computed von Mises stress over pressure in the adventitia layer at an applied lumen pressure (P) of 93mmHg for Patient A where the intraluminal thrombus (ILT) is omitted. The position of the vertebral column (VC) is also indicated.

Patient B:

Next, computed delamination regions for Patient B are analysed when individual wall layer properties are assigned and the ILT is accounted for. A significant region of delamination is predicted at the I-M interface to the right of the vertebral column (VC) as shown in **Figure 13(a)**. The associated interface shear traction evolution for a selection of nodes in the delamination patch are also depicted in **Figure 13(a)**. Following initial interface delamination, computed at 142mmHg in the bottom left quadrant of the delamination patch, the interlayer crack front propagates towards the top right quadrant of the delamination patch following an increase in lumen pressure to 195mmHg. The progression of the interlayer crack front is shown in **Figure 13(b)-(f)** as the lumen pressure is increased from 142mmHg to 195mmHg. The computed σ_{vm}/P distribution in the media layer (when the ILT is included) is presented in **Figure 13(g)**. A selection of nodes in the delamination patch are superimposed for comparison. The initial delamination region, highlighted by circle 'B', does not correlate with a significant σ_{vm}/P concentration. In fact, the computed σ_{vm}/P in this region is relatively low (≈ 0.06MPa). Further increase in lumen pressure causes propagation of the delamination patch longitudinally upwards, eventually reaching a region of high σ_{vm}/P (highlighted by circle 'A'). Crucially, however, delamination initiation does not occur in a region of high σ_{vm}/P.

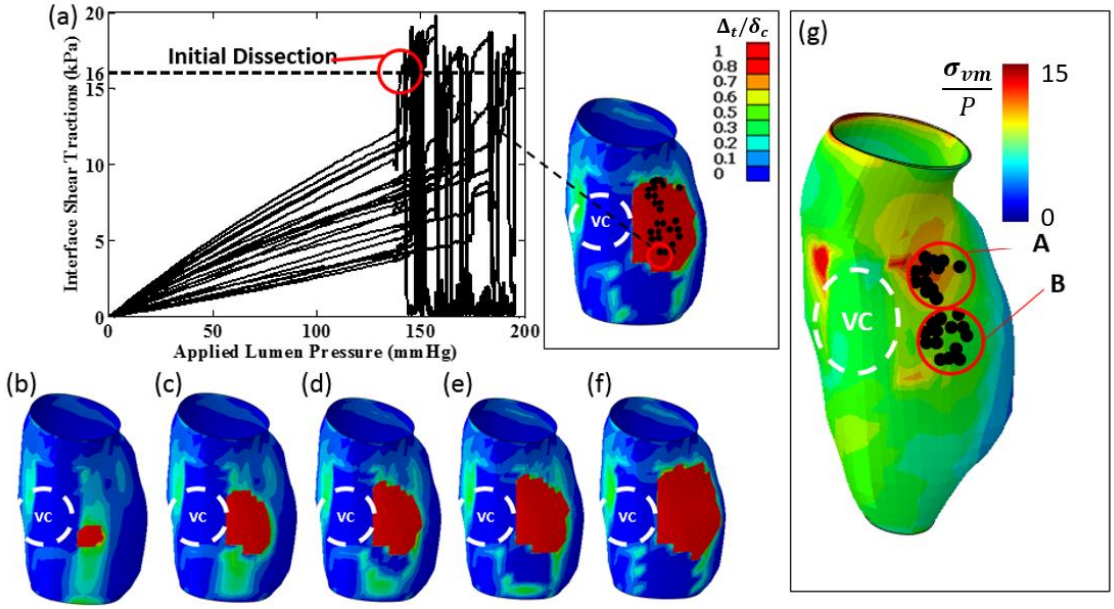

Figure 13: (a) Computed interface shear traction as a function of applied lumen pressure at the intima-media interface for Patient B. A significant region in which the critical cohesive characteristic distance is exceeded ($\Delta_t/\delta_c > 1$) is shown on the right together with the position of the vertebral column (VC). The initial computed delamination region is also indicated. The delamination patch is also shown for a lumen pressure of: (b) 142mmHg; (c) 160mmHg; (d) 170mmHg; (e) 180mmHg and (f) 195mmHg. (g) Distribution of computed σ_{vm}/P in the media layer at an applied lumen pressure (P) of 142mmHg for Patient B. While a region of interlayer delamination (delamination patch A) coincides with peak σ_{vm}/P, the computed region of initial interlayer delamination at the intima-media interface (delamination patch B) does not coincide with region of peak σ_{vm}/P.

Patient C:

Delamination regions for Patient C are analysed next, when inhomogeneous wall layer properties are assigned and the ILT is included in the model. A region of delamination is predicted at the A-M interface just above the position of the vertebral column (VC) as shown in **Figure 14**. The associated shear traction evolution for two nodes in the delamination patch is also depicted. Initial interface delamination is computed at 188mmHg. Following complete interlayer delamination at this node, characterised by a rapid decrease in interface traction, delamination is computed in an adjacent node in the delamination patch at 190mmHg. No interlayer delamination is computed at the I-M interface. The computed σ_{vm}/P distribution in the adventitia layer is presented in **Figure 14(b)** and **Figure 14(c)** for the posterior and anterior AAA sides respectively with the nodes in the delamination patch superimposed for comparison. It is evident that σ_{vm}/P concentrations do not coincide with predicted computed delamination locations. Furthermore, no interlayer delamination is computed on the anterior side where two regions of high σ_{vm}/P are computed.

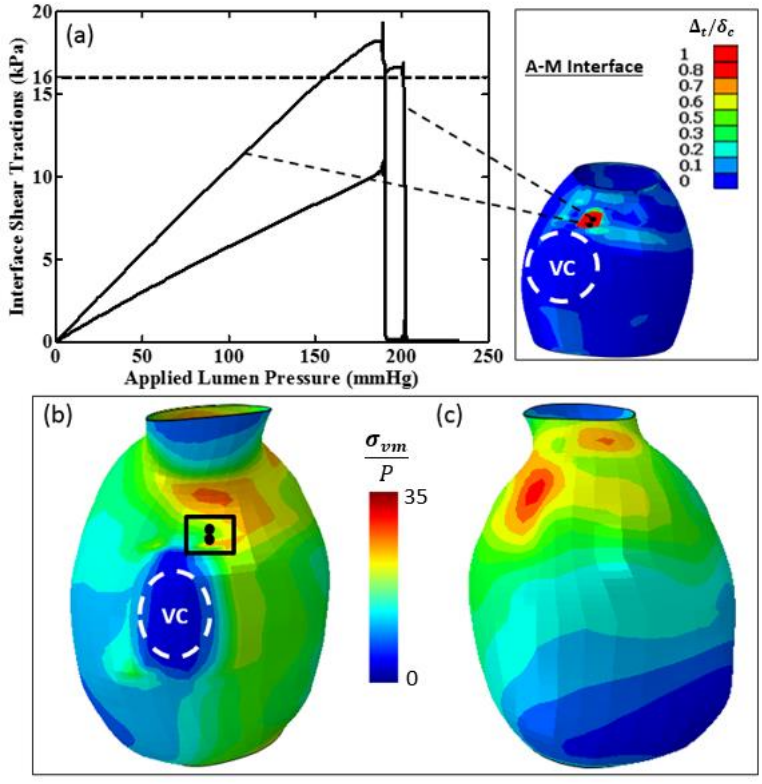

Figure 14: (a) Computed interface shear traction as a function of applied lumen pressure at the adventitia-media interface for Patient C. A significant region in which the critical cohesive characteristic distance is exceeded ($\Delta_t/\delta_c > 1$) is shown on the right together with the position of the vertebral column (VC). (b,c) posterior and anterior distribution of computed σ_{vm}/P in the adventitia layer at an applied lumen pressure of 188mmHg for Patient C where the intraluminal thrombus (ILT) is included. Computed regions of initial interlayer delamination at the adventitia-media do not coincide with region of peak σ_{vm}/P. Individual wall layer properties are chosen for the intima, media, and adventitia layers. The position of the vertebral column (VC) is also indicated.

Conditions Required to Cause I-M Delamination Prior to A-M Delamination

For Patient A, A-M delamination is computed prior to I-M delamination (initial delamination is computed at 132mmHg in the A-M interface as opposed to 138mmHg at the I-M interface). However, it has been observed through CT imaging that dissections primarily occur at the I-M interface in aneurysms (Hyodoh, 1996). Additionally, it has been reported that the intima is a mechanically significant layer of considerable thickness and stiffness for human aged arteries, in contrast to healthy cardiovascular tissue where the intima is relatively thin (Holzapfel, 2007, 2005). Therefore, considering Patient A, an investigation into the conditions which lead to A-M delamination prior to I-M delamination is carried out. Specifically, both the intima thickness and stiffness are doubled. Results are summarised in **Table 1**. As reported above, initial delamination occurs at the lateral right (LR) location of the A-M interface prior to I-M delamination at a lumen pressure of 132mmHg for an intima thickness of 0.17mm and E_{intima}=2.9MPa. I-M delamination is computed at a higher pressure at the lateral right (LR) and anterior bulge (ANT) locations at 138mmHg and 168mmHg, respectively. An increase in intima stiffness to E_{intima}=5.8MPa also results in an initial A-M tear computed at 131mmHg in the lateral right aneurysm location. Interestingly, the increase in intima stiffness also increases the pressure at which I-M delamination is computed in the lateral right location (146mmHg), relative to the less stiff intima. Additionally, for the increased intima stiffness, no delamination is computed in the anterior region of the aneurysm. It is evident in **Table 1** that an increase in intima thickness (0.34mm) significantly reduces the pressure at which I-M delamination are computed, regardless of intima stiffness. Specifically, I-M delamination is computed prior to A-M delamination for E_{intima}=2.9MPa while interlayer delamination are computed at approximately the same pressure for E_{intima}=5.8MPa. Therefore, it is evident that accurate intima stiffness and thickness measurements are crucial in order to accurately predict initial AAA dissection locations.

Table 1: Table summarising the influence of intima thickness and intima stiffness (E_{intima}) on initial delamination pressure and location for Patient A. A-M and I-M refer to the adventitia-media and intima-media interfaces, respectively. Areas LR, LL and ANT refer to lateral right, lateral left, and anterior AAA locations, respectively. All pressures are given in mmHg.

	Intima thickness=0.17mm		**Intima thickness=0.34mm**	
E intima	2.9MPa	5.8MPa	2.9MPa	5.8MPa
A-M	132 **(LR)**	131 **(LR)**	120 **(LR)**	117 **(LR)**
I-M	138 **(LR)** 168 **(ANT)**	146 **(LR)**	115 **(LR)** 111 **(LL)**	118 **(LR)**

Discussion

A key finding of the present study is that the location of delamination initiation does not always coincide with locations of peak σ_{vm} in the artery wall, which suggests that further measures in addition to σ_{vm}, including interface shear strength should be included to improve rupture potential predictions for AAAs. Previous studies have modelled the AAA wall as a single homogenous entity, using the peak computed σ_{vm} as a predictor for rupture (Doyle et al., 2007; Elger, 1996; Inzoli et al., 1993; Mower, 1993; Raghavan, 2000; Raghavan and Vorp, 2000; Stringfellow, 1987; Vorp, 1998). However, the specific rupturing mechanism of the tissue has not been considered in such formulations. Several experimental studies have reported jagged, stepwise mixed-mode failure surfaces of arteries; (FitzGibbon and McGarry, 2020; Brunet et al., 2020; Haslach et al., 2015, 2011; Helfenstein-Didier et al., 2018; Pasta et al., 2012; Purslow, 1983; Romo et al., 2014) indicating that interlayer dissection represents a critical step in the rupture process of AAA tissue and should be considered in computational based RPIs.

Firstly, in order to gain insight into the morphological factors that govern the relationship between peak σ_{vm} and T_t, a parametric investigation is performed on a suite of aneurysm geometries that capture the typical spectrum of AAAs which present clinically. In several cases the location of peak σ_{vm} and T_t coincide, however in a select few there are significant discrepancies between peak locations. Where aneurysm curvature is concerned, a high L/R ratio of 2.5 results in coincident peaks in σ_{vm} and T_t at the aneurysm neck, as the L/R ratio decreases however, the locations of peak σ_{vm} and T_t become non-coincident. The width

of the aneurysm, (W_1), has no effect on the location of peak σ_{vm} nor T_t, only their magnitudes, and they remain coincident as the value of W_1 decreases. Similarly, aneurysm ellipticity has no effect on the coincidence of peak σ_{vm} and T_t as the W_1/W_2 ratio decreases. In the baseline axisymmetric simulation (W_1/W_2=1.00) σ_{vm} and T_t are identical circumferentially at the aneurysm neck, as ellipticity increases (W_1/W_2=[0.90, 0.80]), both σ_{vm} and T_t decrease to a minimum at the minor axis width. Investigation into the skewness of aneurysms reveals that varying the c_{21}/c_{22} ratio does not influence the coincidence of peak σ_{vm} and T_t, however their location follows the greatest curvature at the aneurysm neck. For a symmetric ILT, the location of peak σ_{vm} is non-coincident with the peak T_t location, whereas for an asymmetric ILT, their locations are coincident at the aneurysm neck. Finally, as part of our parametric study we investigated whether the inclusion of anisotropy influences the coincidence of peak σ_{vm} and T_t. The inclusion of an anisotropic material law resulted in a shift of the peak σ_{vm} and T_t from the aneurysm neck to the aneurysm belly, however in both the isotropic and anisotropic case, they remained coincident.

In the second part of this study interlayer delamination is simulated for three AAA geometries reconstructed from patient-specific CT scans. In Patient A delamination initiates at the A-M interface with initial delamination computed at a lumen pressure of 132mmHg. Delamination at the I-M interface initiates at a lumen pressure of 138mmHg. These predictions of delamination initiation are supported by the study of (Fillinger et al., 2002) where AAA rupture is reported at a lumen pressure of 142mmHg, indicating that the assumed values of interface strength are in the correct range for AAA tissue. Interface strengths of up to 140kPa (Ferrara and Pandolfi, 2008; Gasser and Holzapfel, 2006) however have been reported for healthy human tissue, as evident in the fact that healthy tissue does not tend to dissect at pressures as low as 140mmHg. Simulations for Patient B predict delamination initiation at a lumen pressure of 142mmHg, again identical to the rupture pressure reported by (Fillinger et al., 2002). However, the delamination location is very different to that computed for Patient A. In the case of Patient B, delamination initiates in the I-M layer, on the lateral right side of the aneurysm far from the neck region. While delamination initiates at a higher lumen pressure for Patient B, the crack front propagates at a much higher rate than that computed for Patient A, so that a very large delamination patch exists at a lumen pressure of 200mmHg. Finally, initial interlayer delamination is computed at the A-M interface for Patient C at an increased lumen pressure of 188mmHg, with no delamination computed at the I-M interface. The pronounced differences between the delamination predictions, in terms of initiation pressure, location and

crack front propagation highlight the critical importance of understanding geometric variation of AAAs.

The presence of an intraluminal thrombus (ILT) has been reported in approximately 75% of AAAs (Vande Geest, 2006). In addition to the importance of modelling the AAA wall as an inhomogeneous structure, this study also demonstrates the pronounced effect of the ILT on interlayer shear tractions. The presence of the ILT significantly alters the location of interlayer shear traction concentrations in comparison to simulations in which the ILT is excluded. In all cases the removal of the ILT resulted in the prediction of interlayer delamination near the vertebral column. This highlights the importance of the constraining effect of the vertebrae, which results in high concentrations of interlayer tractions if a AAA does not present with an ILT. It is therefore suggested that the vertebral column should be represented in all AAA models. Interestingly, when the ILT was removed from the three patient-specific geometries used in this study, rupture initiated at a lower lumen pressure in all cases relative to simulations in which the ILT was included. The effect of the ILT on AAA wall stress has been reported previously (Doyle et al., 2007; Wang, 2002). The present study furthers emphasises the importance of the ILT in terms of interlayer tractions and delamination prediction in an inhomogeneous wall.

The finding of the present study which shows that delamination locations do not always coincide with locations of σ_{vm} concentrations is broadly supported by the study of Georgakarakos et al., in which it has been reported that aortic blebs, associated with increased risk of rupture, do not correlate with peak σ_{vm} computed for a homogeneous AAA wall (Georgakarakos, 2010). Additionally, Romo et al., (2014) report that rupture locations were not coincident with locations of maximum stress following pressure inflation of thoracic aortic aneurysms. Intimal flaps and false lumens have been reported in the clinical literature for aneurysms, again suggesting that interlayer dissection is an important mode of damage, potentially contributing to total rupture (Hyodoh, 1996; Ring, 2000). Moreover, considering that interface strengths of 140kPa (Gasser and Holzapfel, 2006) and 202kPa (FitzGibbon et al., 2020) have been reported for healthy tissue and that the crack propagation length of aneurysmal tissue is ~3 times that of healthy tissue (Rabin and Haslach, 2018), it is certainly plausible that some factor governing interface strength is compromised in aneurysmal tissue. This is supported by our simulations which reveal that delamination can precede the critical σ_{vm} required to cause rupture using the RPI criterion, highlighting the importance of the inclusion of cohesive zone models into computational based rupture prediction frameworks.

This study has a number of limitations. First of all, passive, hyperelastic materials are assigned to the AAA wall layers and ILT. In reality the remodelling process involved in AAA evolution is a complex one involving the degradation of elastin fibres, increase in collagen crosslinking and a reduction in the contractility of the AAA wall (Carmo, 2002; Henderson, 1999; Lopez-Candales et al., 1997; Rizzo, 1989; Sakalihasan, 1993; Wilson and others, 2001). Important initial steps have been taken to develop an active remodelling constitutive framework to describe the evolution of a AAA (Watton and Hill, 2009; Watton, 2004). Following the prediction of delamination using a cohesive zone approach, inter-layer damage could be simulated using element removal techniques (Feerick and McGarry, 2012). The micro-structural mechanisms of delamination and rupture should also be investigated using micro-mechanical representative volume elements (Dowling et al., 2013; McEvoy et al., 2018) in which the influence of cell contractility on the micro-scale stress distribution is considered (Reynolds et al., 2014; Weafer et al., 2013). More advanced constitutive laws considering cell contractility could also readily be included however it is expected that such detail will not change the stress distribution in the aneurysm wall which is primarily governed by the pressure and wall thickness. Residual stresses, which exist in the AAA wall *in-vivo* (Holzapfel et al., 2000), and wall shear stress induced by blood flow (Peattie, 1996) were also neglected in this study.

In conclusion, delamination locations are not always found to correlate with locations of σ_{vm} concentrations, suggesting that σ_{vm} in the AAA wall should not be relied upon as the sole mechanical indicator of rupture risk, particularly given the experimental evidence of a mixed-mode rupture surface. Furthermore, initial interlayer delamination pressures and locations, in addition to the rate of delamination propagation are found to be highly influenced by the geometric variations. With current AAA rupture risk frameworks only predicting rupture in 53.8% of cases, the addition of cohesive zone models into clinical based FE analyses may improve their accuracy and provide additional information to surgeons in terms of whether the risk of rupture outweighs the risk of surgery for patients.

References

Bellini, C., Kristofik, N.J., Bersi, M.R., Kyriakides, T.R., Humphrey, J.D., 2017. A hidden structural vulnerability in the thrombospondin-2 deficient aorta increases the propensity to intramural delamination. J. Mech. Behav. Biomed. Mater. 71, 397–406. https://doi.org/10.1016/j.jmbbm.2017.01.045

Bersi, M.R., Santamaría, V.A.A., Marback, K., Achille, P. Di, Phillips, E.H., Goergen, C.J., Humphrey, J.D., Avril, S., 2020. Multimodality imaging-Based characterization of Regional Material properties in a Murine Model of Aortic Dissection. https://doi.org/10.1038/s41598-020-65624-7

Brunet, J., Pierrat, B., Adrien, J., Maire, E., Curt, N., Badel, P., 2020. A Novel Method for In Vitro 3D Imaging of Dissecting Pressurized Arterial Segments Using X-Ray Microtomography. Exp. Mech. 1–11. https://doi.org/10.1007/s11340-020-00645-x

Brunet, Joseph, Pierrat, B., Badel, P., 2020. Review of current advances in the mechanical description and quantification of aortic dissection mechanisms. IEEE Rev. Biomed. Eng. 1–1. https://doi.org/10.1109/rbme.2019.2950140

Carmo, M., 2002. Alteration of elastin, collagen and their cross-links in abdominal aortic aneurysms. Eur. J. Vasc. Endovasc. Surg. 23.

Cho, D.Y., Choi, J.H., Kim, B.S., Shin, Y.S., 2019. Comparison of Clinical and Radiologic Outcomes of Diverse Endovascular Treatments in Vertebral Artery Dissecting Aneurysm Involving the Origin of PICA. https://doi.org/10.1016/j.wneu.2018.08.184

Concannon, J., Dockery, P., Black, A., Sultan, S., Hynes, N., McHugh, P.E., Moerman, K.M., McGarry, J.P., 2019. Quantification of the regional bioarchitecture in the human aorta. J. Anat. joa.13076. https://doi.org/10.1111/joa.13076

Darling, R.C., 1977. Autopsy study of unoperated abdominal aortic aneurysms. Circulation 56, 161–164.

Dowling, E.P., Ronan, W., McGarry, J.P., 2013. Computational investigation of in situ chondrocyte deformation and actin cytoskeleton remodelling under physiological loading. Acta Biomater. 9, 5943–5955. https://doi.org/10.1016/j.actbio.2012.12.021

Doyle, B.J., Callanan, A., McGloughlin, T.M., 2007. A comparison of modelling techniques for computing wall stress in abdominal aortic aneurysms. Biomed. Eng. Online 6, 38. https://doi.org/10.1186/1475-925X-6-38

Elger, D.F., 1996. The influence of shape on the stresses in model abdominal aortic aneurysms.

J. Biomech. Eng. 118, 326.

Erhart, P., Roy, J., De Vries, J.P.P.M., Liljeqvist, M.L., Grond-Ginsbach, C., Hyhlik-Dürr, A., Böckler, D., 2016. Prediction of rupture sites in abdominal aortic aneurysms after finite element analysis. J. Endovasc. Ther. 23, 115–120. https://doi.org/10.1177/1526602815612196

Feerick, E.M., McGarry, J.P., 2012. Cortical bone failure mechanisms during screw pullout. J. Biomech. 45, 1666–72. https://doi.org/10.1016/j.jbiomech.2012.03.023

Fereidoonnezhad, B., O'connor, C., Mcgarry, J.P., 2020. A new anisotropic soft tissue model for elimination of unphysical auxetic behaviour. J. Biomech. https://doi.org/10.1016/j.jbiomech.2020.110006

Ferrara, A., Pandolfi, A., 2008. Numerical modelling of fracture in human arteries. Comput. Methods Biomech. Biomed. Engin. 11, 553–567.

Fillinger, M.F., Marra, S.P., Raghavan, M.L., Kennedy, F.E., 2003. Prediction of rupture risk in abdominal aortic aneurysm during observation: wall stress versus diameter. J. Vasc. Surg. 37, 724–32. https://doi.org/10.1067/mva.2003.213

Fillinger, M.F., Raghavan, M.L., Marra, S.P., Cronenwett, J.L., Kennedy, F.E., 2002. In vivo analysis of mechanical wall stress and abdominal aortic aneurysm rupture risk. J. Vasc. Surg. 36, 589–597. https://doi.org/10.1067/mva.2002.125478

FitzGibbon, B., Fereidoonnezhad, B., Concannon, J., Hynes, N., Sultan, S., Moerman, K., McGarry, J., 2020. A numerical investigation of the initiation of aortic dissection. https://doi.org/10.31224/osf.io/g4z72

FitzGibbon, B., McGarry, J.P., 2020. Development of a novel test method to investigate mode II fracture and dissection of arteries. https://doi.org/10.31224/osf.io/d3jbr

Gao, F., Watanabe, M., Matsuzawa, T., 2006. Stress analysis in a layered aortic arch model under pulsatile blood flow. Biomed. Eng. Online 5. https://doi.org/10.1186/1475-925X-5-25

Gasser, T.C., Holzapfel, G.A., 2007. Modeling plaque fissuring and dissection during balloon angioplasty intervention. Ann. Biomed. Eng. 35, 711–723.

Gasser, T.C., Holzapfel, G.A., 2006. Modeling the propagation of arterial dissection. Eur. J. Mech. A/Solids 25, 617–633. https://doi.org/10.1016/j.euromechsol.2006.05.004

Georgakarakos, E., 2010. Peak wall stress does not necessarily predict the location of rupture in abdominal aortic aneurysms. Eur. J. Vasc. Endovasc. Surg. 39, 302–304.

Hakimi, R., Sivakumar, S., 2019. Imaging of Carotid Dissection. https://doi.org/10.1007/s11916-019-0741-9

Hall, A.J., 2000. Aortic wall tension as a predictive factor for abdominal aortic aneurysm rupture: improving the selection of patients for abdominal aortic aneurysm repair. Ann. Vasc. Surg. 14, 152–157.

Haslach, H.W., Leahy, L.N., Fathi, P., Barrett, J.M., Heyes, A.E., Dumsha, T.A., Mcmahon, E.L., 2015. Crack Propagation and Its Shear Mechanisms in the Bovine Descending Aorta. Cardiovasc. Eng. Technol. 6. https://doi.org/10.1007/s13239-015-0245-7

Haslach, H.W., Riley, P., Molotsky, A., 2011. The Influence of Medial Substructures on Rupture in Bovine Aortas. Cardiovasc. Eng. Technol. 2, 372–387. https://doi.org/10.1007/s13239-011-0056-4

Haslach, H.W., Siddiqui, A., Weerasooriya, A., Nguyen, R., Roshgadol, J., Monforte, N., McMahon, E., 2018. Fracture mechanics of shear crack propagation and dissection in the healthy bovine descending aortic media. Acta Biomater. 68, 53–66. https://doi.org/10.1016/j.actbio.2017.12.027

Helfenstein-Didier, C., Taïnoff, D., Viville, J., Adrien, J., Maire, É., Badel, P., 2018. Tensile rupture of medial arterial tissue studied by X-ray micro-tomography on stained samples. J. Mech. Behav. Biomed. Mater. 78, 362–368. https://doi.org/10.1016/j.jmbbm.2017.11.032

Henderson, E.L., 1999. Death of smooth muscle cells and expression of mediators of apoptosis by T lymphocytes in human abdominal aortic aneurysms. Circulation 99, 96.

Hirst, A.E., Johns, V.J., Kime, S.W., 1958. Dissecting aneurysm of the aorta: A review of 505 cases. Med. (United States). https://doi.org/10.1097/00005792-195809000-00003

Holzapfel, G.A., 2007. Layer-specific 3D residual deformations of human aortas with non-atherosclerotic intimal thickening. Ann. Biomed. Eng. 35, 530–545.

Holzapfel, G.A., 2005. Determination of layer-specific mechanical properties of human coronary arteries with nonatherosclerotic intimal thickening and related constitutive modeling. Am. J. Physiol. Circ. Physiol. 289.

Holzapfel, G.A., Gasser, T.C., Ogden, R.W., 2000. A New Constitutive Framework for Arterial Wall Mechanics and a Comparative Study of Material Models. J. Elast. Phys. Sci. solids 61, 1–48. https://doi.org/10.1023/A:1010835316564

Hyodoh, H., 1996. Three-dimensional CT imaging of an isolated dissecting aneurysm of the superior mesenteric artery. Abdom. Imaging 21, 515–516.

Inzoli, F., Boschetti, F., Zappa, M., Longo, T., Fumero, R., 1993. Biomechanical factors in abdominal aortic aneurysm rupture. Eur. J. Vasc. Surg. 7, 667–74.

Kazi, M., Thyberg, J., Religa, P., Roy, J., Eriksson, P., Hedin, U., Swedenborg, J., 2003.

Influence of intraluminal thrombus on structural and cellular composition of abdominal aortic aneurysm wall. J. Vasc. Surg. 38, 1283–1292. https://doi.org/10.1016/S0741-5214(03)00791-2

Kim, J.-H., Avril, S., Duprey, A., Favre, J.-P., 2012. Experimental characterization of rupture in human aortic aneurysms using a full-field measurement technique. Biomech Model Mechanobiol 11, 841–853. https://doi.org/10.1007/s10237-011-0356-5

Kohn, J.C., Lampi, M.C., Reinhart-King, C.A., 2015. Age-related vascular stiffening: causes and consequences. Front. Genet. 6, 112. https://doi.org/10.3389/fgene.2015.00112

Kontopodis, N., Pantidis, D., Dedes, A., Daskalakis, N., Ioannou, C. V, 2016. The - Not So - Solid 5.5 cm Threshold for Abdominal Aortic Aneurysm Repair: Facts, Misinterpretations, and Future Directions. Front. Surg. 3, 1. https://doi.org/10.3389/fsurg.2016.00001

Leung, J.H., Wright, A.R., Cheshire, N., Crane, J., Thom, S.A., Hughes, A.D., Xu, Y., 2006. Fluid structure interaction of patient specific abdominal aortic aneurisms: A comparison with solid stress models. Biomed. Eng. Online 5, 1–15. https://doi.org/10.1186/1475-925X-5-33

Li, X., Zhao, G., Zhang, J., Duan, Z., Xin, S., 2013. Prevalence and trends of the abdominal aortic aneurysms epidemic in general population-a meta-analysis. PLoS One 8, 81260. https://doi.org/10.1371/journal.pone.0081260

Lopez-Candales, A., Holmes, D.R., Liao, S., Scott, M.J., Wickline, S.A., Thompsontt, R.W., 1997. Decreased Vascular Smooth Muscle Cell Density in Medial Degeneration of Human Abdominal Aortic Aneurysms, Americat Journal of Pathology.

Máirtín, É.Ó., Parry, G., Beltz, G.E., McGarry, J.P., 2014. Potential-based and non-potential-based cohesive zone formulations under mixed-mode separation and over-closure-Part II: Finite element applications. J. Mech. Phys. Solids 63, 363–385. https://doi.org/10.1016/j.jmps.2013.08.019

Maus, V., Mpotsaris, A., Dorn, F., Mö Hlenbruch, M., Borggrefe, J., Stavrinou, P., Abdullayev, N., Barnikol, U.B., Liebig, T., Kabbasch, C., 2018. The Use of Flow Diverter in Ruptured, Dissecting Intracranial Aneurysms of the Posterior Circulation. https://doi.org/10.1016/j.wneu.2017.12.095

McEvoy, E., Holzapfel, G.A., McGarry, P., 2018. Compressibility and Anisotropy of the Ventricular Myocardium: Experimental Analysis and Microstructural Modeling. J. Biomech. Eng. 140. https://doi.org/10.1115/1.4039947

McGarry, J.P., Ó Máirtín, É., Parry, G., Beltz, G.E., 2014. Potential-based and non-potential-

based cohesive zone formulations under mixed-mode separation and over-closure. Part I: Theoretical analysis. J. Mech. Phys. Solids 63, 336–362. https://doi.org/10.1016/j.jmps.2013.08.020

Moerman, K.M., 2018. GIBBON: The Geometry and Image-Based Bioengineering add-On. J. Open Source Softw. 3, 506. https://doi.org/10.21105/joss.00506

Mower, W.R., 1993. Stress distributions in vascular aneurysms: factors affecting risk of aneurysm rupture. J. Surg. Res. 55, 155.

Pasta, S., Phillippi, J.A., Gleason, T.G., Vorp, D.A., 2012. Effect of aneurysm on the mechanical dissection properties of the human ascending thoracic aorta. J. Thorac. Cardiovasc. Surg. 143, 460–467. https://doi.org/10.1016/j.jtcvs.2011.07.058

Peattie, R.A., 1996. Steady flow in models of abdominal aortic aneurysms Part II: Wall stresses and their implication for in vivo thrombosis and rupture. J. ultrasound Med. 15, 689–696.

Phillips, E.H., Achille, P. Di, Bersi, M.R., Humphrey, J.D., Goergen, C.J., 2017. Multi-Modality Imaging Enables Detailed Hemodynamic Simulations in Dissecting Aneurysms in Mice HHS Public Access. IEEE Trans Med Imaging 36, 1297–1305. https://doi.org/10.1109/TMI.2017.2664799

Polzer, S., Gasser, T.C., 2015. Biomechanical rupture risk assessment of abdominal aortic aneurysms based on a novel probabilistic rupture risk index. J. R. Soc. Interface 12. https://doi.org/10.1098/rsif.2015.0852

Purslow, P.P., 1983a. Positional variations in fracture toughness, stiffness and strength of descending thoracic pig aorta. J. Biomech. 16, 947–953. https://doi.org/10.1016/0021-9290(83)90058-1

Purslow, P.P., 1983b. Positional variations in fracture toughness, stiffness and strength of descending thoracic pig aorta. J. Biomech. 16, 947–953. https://doi.org/10.1016/0021-9290(83)90058-1

Rabin, J., Haslach, H.W., 2018. IN-VITRO MODEL OF MINOR AORTIC INJURY DEMONSTRATES SHEAR FORCES FACILITATING AORTIC CRACK PROPAGATION [WWW Document]. Acad. Surg. Congr. Abstr. Arch. URL https://www.asc-abstracts.org/abs2018/41-16-in-vitro-model-of-minor-aortic-injury-demonstrates-shear-forces-facilitating-aortic-crack-propagation/ (accessed 11.10.20).

Raghavan, M.L., 2000. Wall stress distribution on three-dimensionally reconstructed models of human abdominal aortic aneurysm. J. Vasc. Surg. 31, 760–769.

Raghavan, M.L., Vorp, D.A., 2000. Toward a biomechanical tool to evaluate rupture potential of abdominal aortic aneurysm: identification of a finite strain constitutive model and

evaluation of its applicability. J. Biomech. 33, 475–482.

Reynolds, N.H., Ronan, W., Dowling, E.P., Owens, P., McMeeking, R.M., McGarry, J.P., 2014. On the role of the actin cytoskeleton and nucleus in the biomechanical response of spread cells. Biomaterials 35, 4015–4025. https://doi.org/10.1016/j.biomaterials.2014.01.056

Ring, W.S., 2000. Congenital Heart Surgery Nomenclature and Database Project: aortic aneurysm, sinus of Valsalva aneurysm, and aortic dissection. Ann. Thorac. Surg. 69, 147–163.

Rizzo, R.J., 1989. Collagen types and matrix protein content in human abdominal aortic aneurysms. J. Vasc. Surg. Off. Publ. Soc. Vasc. Surg. [and] Int. Soc. Cardiovasc. Surgery, North Am. Chapter 10, 365.

Romo, A., Badel, P., Duprey, A., Favre, J.-P., Avril, S., 2014. In vitro analysis of localized aneurysm rupture. J. Biomech. 47, 607–16. https://doi.org/10.1016/j.jbiomech.2013.12.012

Sakalihasan, N., 1993. Modifications of the extracellular matrix of aneurysmal abdominal aortas as a function of their size. Eur. J. Vasc. Surg. 7, 633.

Schriefl, A.J., Collins, M.J., Pierce, D.M., Holzapfel, G.A., Niklason, L.E., Humphrey, J.D., 2012. Remodeling of Intramural Thrombus and Collagen in an Ang-II Infusion ApoE−/− Model of Dissecting Aortic Aneurysms. https://doi.org/10.1016/j.thromres.2012.04.009

Sommer, G., 2008. Dissection Properties of the Human Aortic Media: An Experimental Study. J. Biomech. Eng. 130, 21007.

Speelman, L., Schurink, G.W.H., Bosboom, E.M.H., Buth, J., Breeuwer, M., van de Vosse, F.N., Jacobs, M.H., 2010. The mechanical role of thrombus on the growth rate of an abdominal aortic aneurysm. J. Vasc. Surg. 51, 19–26. https://doi.org/10.1016/j.jvs.2009.08.075

Stringfellow, M.M., others, 1987. The influence of aorta-aneurysm geometry upon stress in the aneurysm wall. J Surg Res 42, 425–433.

Sugita, S., Matsumoto, · Takeo, 2018. Local distribution of collagen fibers determines crack initiation site and its propagation direction during aortic rupture. Biomech Model Mechanobiol 17, 577–587. https://doi.org/10.1007/s10237-017-0979-2

Teng, Z., Feng, J., Zhang, Y., Huang, Y., Sutcliffe, M.P.F., Brown, A.J., Jing, Z., Gillard, J.H., Lu, Q., 2015. Layer- and Direction-Specific Material Properties, Extreme Extensibility and Ultimate Material Strength of Human Abdominal Aorta and Aneurysm: A Uniaxial Extension Study. Ann. Biomed. Eng. 43, 2745–2759. https://doi.org/10.1007/s10439-

015-1323-6

Trachet, B., Aslanidou, L., Piersigilli, A., Fraga-Silva, R.A., Sordet-Dessimoz, J., Villanueva-Perez, P., Stampanoni, M.F.M., Stergiopulos, N., Segers, P., 2017. Angiotensin II infusion into ApoE-/-mice: a model for aortic dissection rather than abdominal aortic aneurysm? https://doi.org/10.1093/cvr/cvx128

Vande Geest, J., 2006. A planar biaxial constitutive relation for the luminal layer of intra-luminal thrombus in abdominal aortic aneurysms. J. Biomech. 39, 2347–2354.

Vande Geest, Jonathan P, Di Martino, E.S., Bohra, A., Makaroun, M.S., Vorp, D.A., 2006. A biomechanics-based rupture potential index for abdominal aortic aneurysm risk assessment: demonstrative application. Ann. N. Y. Acad. Sci. 1085, 11–21. https://doi.org/10.1196/annals.1383.046

Vande Geest, Jonathan P., Sacks, M.S., Vorp, D.A., 2006. The effects of aneurysm on the biaxial mechanical behavior of human abdominal aorta. J. Biomech. 39, 1324–1334. https://doi.org/10.1016/J.JBIOMECH.2005.03.003

Venkatasubramaniam, A.K., Fagan, M.J., Mehta, T., Mylankal, K.J., Ray, B., Kuhan, G., Chetter, I.C., McCollum, P.T., 2004. A comparative study of aortic wall stress using finite element analysis for ruptured and non-ruptured abdominal aortic aneurysms. Eur. J. Vasc. Endovasc. Surg. 28, 168–176. https://doi.org/10.1016/j.ejvs.2004.03.029

Vorp, D.A., 2007. Biomechanics of abdominal aortic aneurysm. J. Biomech. 40, 1887–1902.

Vorp, D.A., 1998. Mechanical wall stress in abdominal aortic aneurysm: influence of diameter and asymmetry. J. Vasc. Surg. 27, 632–639.

Vorp, D.A., Vande Geest, J., 2005. Biomechanical determinants of abdominal aortic aneurysm rupture. Arterioscler. Thromb. Vasc. Biol. 25, 1558–1566.

Wang, D.H.J., 2002. Effect of intraluminal thrombus on wall stress in patient-specific models of abdominal aortic aneurysm. J. Vasc. Surg. 36, 598–604.

Wang, D.H.J., 2001. Mechanical properties and microstructure of intraluminal thrombus from abdominal aortic aneurysm. J. Biomech. Eng. 123, 536.

Watton, P.N., Hill, N.A., 2009. Evolving mechanical properties of a model of abdominal aortic aneurysm. Biomech. Model. Mechanobiol. 8, 25–42. https://doi.org/10.1007/s10237-007-0115-9

Watton, P.N., others, 2004. A mathematical model for the growth of the abdominal aortic aneurysm. Biomech. Model. Mechanobiol. 3, 98–113.

Weafer, P.P., Ronan, W., Jarvis, S.P., McGarry, J.P., 2013. Experimental and Computational Investigation of the Role of Stress Fiber Contractility in the Resistance of Osteoblasts to

Compression. Bull. Math. Biol. 75, 1284–1303. https://doi.org/10.1007/s11538-013-9812-y

Wilson, K.A., others, 2001. The Relationship Between Abdominal Aortic Aneurysm Distensibility and Serum Markers of Elastin and Collagen Metabolism. Eur. J. Vasc. Endovasc. Surg. 21, 175–178.

Xanthoulea, S., Thelen, M., Pö Ttgens, C., Gijbels, M.J.J., Lutgens, E., De Winther, M.P.J., 2009. Absence of p55 TNF Receptor Reduces Atherosclerosis, but Has No Major Effect on Angiotensin II Induced Aneurysms in LDL Receptor Deficient Mice. https://doi.org/10.1371/journal.pone.0006113

Xenos, M., Labropoulos, N., Rambhia, S., Alemu, Y., Einav, S., Tassiopoulos, A., Sakalihasan, N., Bluestein, D., 2014. Progression of Abdominal Aortic Aneurysm Towards Rupture: Refining Clinical Risk Assessment Using a Fully Coupled Fluid–Structure Interaction Method. Ann. Biomed. Eng. 43, 139–153. https://doi.org/10.1007/s10439-014-1224-0